

# Shape optimisation of the sharp-heeled Kaplan draft tube: Part I - performance evaluation using Computational Fluid Dynamics

S. J. Daniels<sup>a</sup>, A. A. M. Rahat<sup>b</sup>, G. R. Tabor<sup>a</sup>, J. E. Fieldsend<sup>a</sup>, R. M. Everson<sup>a</sup>

<sup>a</sup>*College of Engineering, Mathematics and Physical Sciences, University of Exeter*

<sup>b</sup>*School of Computing, Electronics and Mathematics, University of Plymouth*

---

## Abstract

1 In the first of this two-part contribution, a methodology to assess the perfor-  
2 mance of an elbow-type draft tube is outlined. using Computational Fluid  
3 Dynamics (CFD) to evaluate the pressure recovery and mechanical energy  
4 losses along a draft tube design, while using open-source and commercial  
5 software to parameterise and regenerate the geometry and CFD grid. An  
6 initial validation study of the elbow-type draft tube is carried out, focusing  
7 on the grid-regeneration methodology, and the use of a steady-state assump-  
8 tion for evaluating the design's efficiency. The Grid Convergence Index (GCI)  
9 technique was used to assess the uncertainty of the pressure recovery to the  
10 grid resolution. It was found that estimating the pressure recovery through  
11 area-weighted averaging significantly reduced the uncertainty due to the grid.  
12 Simultaneously, it was found that this uncertainty fluctuated with the local  
13 cross-sectional area along the geometry. Subsequently, a study of the inflow  
14 cone and outer-heel designs on the flowfield and pressure recovery was car-  
15 ried out. Catmull-Rom splines were used to parameterise these components,  
16 so as to recreate a number of proposed designs from the literature. GCI  
17 analysis is also applied to these designs, demonstrating the robustness of the  
18 grid-regeneration methodology.

*Keywords:* Hölleforsen-Kaplan draft tube, Pressure recovery, Grid Convergence Index, cfMesh, Catmull-Rom Splines.

---

*Email address:* S.Daniels@exeter.ac.uk (S. J. Daniels)

19 **1. Introduction**

20 The performance of a hydraulic turbine is significantly affected by the  
21 efficiency of its draft tube, which serves the following functions:

- 22 • to recover energy, by converting some of the kinetic energy leaving the  
23 runner into static head that would otherwise be lost in the absence of  
24 a draft tube;
- 25 • to position the turbine runner above or below the tail water level to  
26 avoid cavitation, without affecting the net-head.

27 Several factors make the design of the draft tube a daunting task. The flow  
28 itself, largely decelerating, is subject to viscous turbulent effects (such as flow  
29 separation) which reduce its effectiveness. To make matters worse, some de-  
30 signs are often made more complicated by the inclusion of an approximately  
31  $90^\circ$  bend (elbow-type) to improve powerhouse compactness and to minimise  
32 construction costs. Furthermore, the outflow cross-section is often rectangu-  
33 lar, while the inflow cross-section is circular to couple with the runner. Thus,  
34 the geometry of the draft tube design needs to be thought out very carefully  
35 to achieve the best possible compromise between hydraulic efficiency and  
36 construction costs. This leads to a large number of design parameters which  
37 could potentially be changed to alter and optimise its efficiency.

38 Fundamentally, factors which alter the draft tube's performance are its ge-  
39 ometrical shape, and the velocity distribution (profiles) at the inflow. So far,  
40 the design of the draft tube has been tempered through experimental obser-  
41 vations and semi-empirical formulae of established geometries (notably: [1]).  
42 To explore potential new designs, Computational Fluid Dynamics (CFD)  
43 has proved to be a powerful tool for the engineer, allowing for comprehen-  
44 sive analysis of complex flowfields where experimental work provides limited  
45 insight. CFD becomes especially appealing when combined with a global  
46 optimisation method which may significantly reduce the number of evalua-  
47 tions during the design cycle. Consequently, there is a need for developing an  
48 accurate and robust CFD approach, together with an efficient optimisation  
49 strategy.

50 Parameter-based shape optimisation is based on the philosophy that, any  
51 geometry in all its complexity and details, can be described by a group of  
52 parameters (control points), allowing the geometry to be suitably modified  
53 to improve its performance. Through this approach, it is easy to co-relate the

54 impact of a parameter’s value on the design objectives. More importantly,  
55 this approach allows the exploration of large global design spaces without  
56 any conceptual barriers. However, cases involving such unconstrained de-  
57 sign spaces may result in complex geometries, potentially compromising the  
58 accuracy of the objective functions depending on the fidelity of the CFD  
59 methodology.

60 CFD requires the solution of a set of Partial Differential Equations (PDEs)  
61 describing the physics of fluid flow. This is typically achieved using a dis-  
62 cretisation method, in which a grid is constructed across the fluid continuum,  
63 and the PDEs are solved algebraically within each cell. Cell quality issues  
64 can impede the accuracy of the eventual solution, even to the point where  
65 the solver diverges and no solution is generated; they can also significantly  
66 affect the level of computational work (i.e. number of iterations) necessary to  
67 reach the solution. Thus, grid generation is commonly recognised as one of  
68 the main challenges in CFD, which in itself has motivated the use of optimi-  
69 sation techniques to improve the overall grid quality (e.g. [2]). Moreover, for  
70 automated shape optimisation, large perturbations of the geometry’s surface  
71 will require the Computer-Aided Design (CAD) model and CFD grid to be  
72 reconstructed for each evaluation (e.g. [3, 4, 5]), rather than redistribute the  
73 existing grid within the domain. However, despite their potential, reports  
74 on the application and efficacy of automated CAD and grid regeneration  
75 techniques for shape optimisation are largely absent in the literature.

76 In the context of draft tube shape optimisation, reports have often em-  
77 ployed the use of commercial software to reconstruct the CAD and grid for  
78 each evaluation. Marjavaara and Lundström [6] and Hellström et al. [7]  
79 investigated the heel curvature effects on the draft tube efficiency using the  
80 commercial software I-deas NX 10 and ICEM CFD Hexa to construct the  
81 CAD geometry and CFD grid respectively. While grid sensitivity analysis  
82 was carried out, neither the topology of their base grid or method of refine-  
83 ment were reported. Galván et al. [8] employed ANSYS Fluent to construct  
84 a block-structured grid while uniformly refining all vertices for their sen-  
85 sitivity study. The above papers employ Richardson extrapolation of the  
86 grid–solution convergence to estimate the uncertainty [9, 10]. However, they  
87 report oscillating convergence issues (possibly indicating a topological prob-  
88 lem within the grid [11, 12]) – the nature of these issues remains uncertain.  
89 With an increasing interest in automatically optimising the shape of the draft  
90 tube with more unconventional design features (see [13]), the sensitivity of  
91 the CFD grid resolution for these draft tube designs should be investigated.

92 Thus, in the present work, the use of an open-source grid regenerator and  
93 consistent CFD methodology is used to assess the efficiency of number of  
94 proposed draft tube designs from the literature, and to gain a deeper insight  
95 into the uncertainty of the results to the grid resolution. Overall, this analy-  
96 sis will aid future CFD applications to draft tube designs in association with  
97 automated shape optimisation.

### 98 *1.1. Base draft tube geometry*

99 Elbow-type draft tubes are widely used in conjunction with vertical Ka-  
100 plan and Francis turbines, due to their lower excavation cost and greater  
101 potential for pressure recovery. The two most common draft tube designs  
102 reported in the literature are the sharp-heeled (e.g., [14, 15]), and under-  
103 ground (e.g. [16]) types. The former encompasses a large group of draft  
104 tubes that were installed in Swedish hydropower plants during the 1950s.  
105 The base geometry considered in the present work is a 1:11 scaled model  
106 of the Hölleforsen-Kaplan draft tube, constructed in 1949. This design has  
107 served extensively as a benchmark test case for both experimental and nu-  
108 merical studies in the literature – largely through the European Research  
109 Community On Flow, Turbulence And Combustion (ERCOFTAC) Turbine-  
110 99 Workshop series [17, 14, 18]. A schematic of the draft tube geometry is  
111 shown in Fig.1.

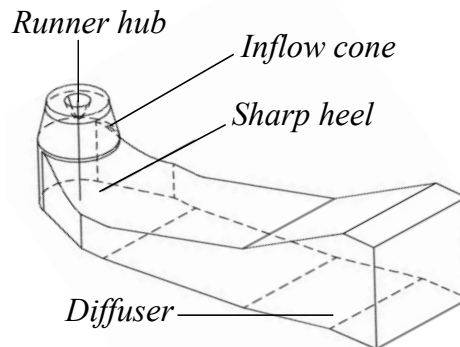


Figure 1: Schematic of the sharp-heeled Hölleforsen-Kaplan draft tube.

### 112 *1.2. Paper Overview*

113 With the overarching aim to improve the draft tube performance over two  
114 consecutive papers, this first contribution will address the following topics:

- 115 • to examine the draft tube efficiency based on the method of estimation;
- 116 • to investigate the performance of proposed designs for the elbow-type  
117 draft tube;
- 118 • to assess the uncertainty of performance measures relating to the grid  
119 resolution for various draft tube designs.

120 The structure of this paper reflects the stages of work undertaken to-  
121 wards achieving the above goals. §2 outlines the overall methodology used  
122 for assessing the flow through the draft tube, starting with the simulation  
123 setup in §2.1. The methods of measuring the performance of the draft tube  
124 is outlined in §2.2. This is followed by the methodology for the automatic  
125 grid regeneration in §2.3. The proposed CFD methodology is subsequently  
126 validated using the sharp-heeled Hölleforsen-Kaplan draft tube in §2.4 with a  
127 discussion concerning the 1st topic and overall fidelity of the CFD approach.  
128 This is examined further in §2.5 in which the Grid Convergence Index (GCI)  
129 method [12] is used to estimate the uncertainty associated to the grid resolu-  
130 tion. §3 applies the above CFD methodology to a number of proposed draft  
131 tube designs from the literature. A study of the inflow cone and outer-heel  
132 design on the draft tube performance is carried out in §3.1 and §3.2 respec-  
133 tively, addressing the 2nd topic of this paper. GCI analysis is also applied  
134 to these designs following the 3rd topic. Finally, in §4, the observations, and  
135 premise for future work are summarised.

## 136 2. Numerical methodology

### 137 2.1. CFD setup

138 The CFD simulations in this work were performed using the open-source  
139 C++ code OpenFOAM-4.x. Since its public release in 2004, OpenFOAM has  
140 been the subject of many validation publications, including the flow through  
141 the draft tube considered in this work (e.g. [19, 20]). The fluid flow was mod-  
142 elled using the Reynolds-Averaged Navier-Stokes (RANS) equations. These  
143 equations can be derived by substituting mean and fluctuating components  
144 of the flowfield variables into the incompressible Navier-Stokes equations:

145 The continuity equation:

$$\frac{\partial U_i}{\partial x_i} = 0. \tag{1}$$

146 The momentum equations:

$$\frac{\partial U_i}{\partial t} + U_j \frac{\partial U_i}{\partial x_j} = -\frac{\partial \bar{p}/\rho}{\partial x_i} + \nu \frac{\partial^2 U_i}{\partial x_j \partial x_j} - \frac{\partial}{\partial x_j} (\overline{u'_i u'_j}), \quad (2)$$

147 where

$$\overline{u'_i u'_j} = \nu_t \left( \frac{\partial U_i}{\partial x_j} + \frac{\partial U_j}{\partial x_i} \right) - \frac{1}{3} \overline{u'_i u'_i} \delta_{ij}. \quad (3)$$

148  $U$  and  $\bar{p}$  are the averaged velocity and static pressure respectively, and  
 149  $u'$  is the fluctuating component of velocity.  $\rho$  and  $\nu$  are the density and  
 150 kinematic viscosity of the fluid. The standard  $k - \epsilon$  model was used for the  
 151 calculation of the turbulent viscosity by the relation  $\nu_t = C_\mu k^2/\epsilon$ , where  $k$   
 152 is the turbulent kinetic energy, and  $\epsilon$  is the rate of dissipation. The  $k$  and  $\epsilon$   
 153 transport equations are described:

$$\frac{\partial k}{\partial t} + \frac{\partial}{\partial x_i} (U_i k) = \frac{\partial}{\partial x_j} \left[ \left( \nu + \frac{\nu_t}{\sigma_k} \right) \frac{\partial k}{\partial x_j} \right] - \overline{u'_i u'_j} \frac{\partial U_j}{\partial x_i} - \epsilon, \quad (4)$$

154

$$\frac{\partial \epsilon}{\partial t} + \frac{\partial}{\partial x_i} (U_i \epsilon) = \frac{\partial}{\partial x_j} \left[ \left( \nu + \frac{\nu_t}{\sigma_\epsilon} \right) \frac{\partial \epsilon}{\partial x_j} \right] - \frac{\epsilon}{k} \left( C_{1\epsilon} \overline{u'_i u'_j} \frac{\partial U_j}{\partial x_i} + C_{2\epsilon} \epsilon \right), \quad (5)$$

155 where the associated empirical coefficients are defined in Table 1.

$C_{1\epsilon}$	$C_{2\epsilon}$	$C_\mu$	$\sigma_k$	$\sigma_\epsilon$
1.44	1.92	0.09	1	1.3

Table 1: Empirical constants for used for the standard  $k - \epsilon$  turbulence model.

156 The suitability of the  $k - \epsilon$  turbulence model in simulating the swirling  
 157 flow and near-wall modelling along the draft tube has been extensively stud-  
 158 ied in the Turbine-99 workshop series and independent publications (e.g.  
 159 [18, 21, 22, 13]). The Finite Volume Method was used to integrate the above  
 160 equations [23]. The second-order central difference scheme was used to discre-  
 161 tise the diffusion terms, and the second-order upwind difference was adopted  
 162 for the convection term. For the unsteady simulations, a first-order implicit  
 163 scheme (Euler) for the temporal discretisation was employed; in such cases,  
 164 the PISO algorithm [24] was adopted for the velocity-pressure coupling, with

165 the number of pressure correctors set to 2. For the steady-state calcula-  
 166 tions, the SIMPLE algorithm [25] was used, with under-relaxation factors  
 167 0.7, 0.3, and 0.7 for the velocity, pressure, and turbulence quantities respec-  
 168 tively. The generalised Geometric-Algebraic Multi-Grid solver was used to  
 169 solve the pressure field, while the Gauss-Seidel linear solver was used for the  
 170 remaining field variables.

171 The boundary conditions in the present work are chosen to reproduce those  
 172 specified by the organisers of the 2nd Turbine-99 Workshop [14]. At the  
 173 outflow, all field variables, excluding pressure, are specified as a zero-normal  
 174 gradient, i.e., it is assumed that the field is fully developed at the outlet.  
 175 Moreover, an extension to the outflow of  $2m$  was applied to the geometry to  
 176 avoid any backflow at the outflow plane, and to ensure convergence of the  
 177 solution. For the draft tube walls, a no-slip condition is applied for the veloc-  
 178 ity, and a zero-normal gradient condition for pressure; a rotational velocity  
 179 was applied to the runner-hub in accordance to the turbine rotation. At the  
 180 inflow, a swirl flow was imposed to represent the discharge from the Kaplan  
 181 turbine. The axial ( $U$ ) and tangential ( $W$ ) velocity components from Laser-  
 182 Doppler-Anemometry (LDA) measurements [14, 26] are linearly interpolated  
 183 onto the CFD boundary. Data for the radial velocity, Reynolds stresses, and  
 184 turbulent length scales were not reported and had to be approximated. The  
 185 radial velocity ( $V$ ) distribution at the inflow was assumed to be attached to  
 186 the runner-hub and the draft tube walls, as described through the function  
 187 proposed by Cervantes et al. [18]:

$$V(r) = U(r) \tan(\theta), \quad (6)$$

188 where

$$\theta = \theta_{cone} + \left( \frac{\theta_{wall} - \theta_{cone}}{R_{wall} - R_{cone}} \right) (r - R_{cone}), \quad (7)$$

189 with  $R_{cone} \leq r \leq R_{wall}$ ,  $\theta_{cone} = -12.8^\circ$  and  $\theta_{wall} = 2.8^\circ$  for the geometry  
 190 considered [18]. The unknown turbulent quantities at the inflow are assumed:  
 191  $\overline{v'v'} = \overline{w'w'}$ , and  $\overline{u'u'} = \overline{u'v'} = \overline{u'w'}$  in accordance to the modelling specifications  
 192 provided in the 2nd Turbine-99 workshop [14]. The quantities for  $k$  and  $\epsilon$  at  
 193 the inflow boundary were estimated by the following expressions:

$$k = \frac{1}{2} (\overline{u'_i u'_i}) = \frac{3}{2} \left( \left( \frac{Q}{A_{in}} \right) I \right)^2, \quad (8)$$

194

$$\epsilon = \frac{C_\mu^{\frac{3}{4}} k^{\frac{3}{2}}}{l_\epsilon}; \quad l_\epsilon = 0.1(R_{wall} - R_{cone}), \quad (9)$$

195 where  $Q$  and  $A_{in}$  are the volumetric discharge and cross-sectional area of  
 196 the inflow, and  $I = u'/(Q/A_{in})$  is the turbulence intensity – estimated as  
 197 10% from the experimental data by Andersson and Cervantes [26].  $l_\epsilon$  is a  
 198 constant length scale, recommended to be between 1–10% of the hydraulic  
 199 diameter [27, 14]. The operating conditions for the Kaplan turbine were set  
 200 at the ‘ $T(n)$ ’ mode [18] detailed in Table 2.

Operating Condition	$N$ (rpm)	$Q$ ( $m^3/s$ )	$Re_D$ ( $10^6$ )
$T(n)$	595	0.522	1.329

Table 2: Kaplan turbine operating mode ‘ $T(n)$ ’.  $N$  is the rotational speed of the turbine, and Reynolds number  $Re_D = (Q/A_{in})D_0/\nu$  ( $D_0 = 0.5m$  [14]).

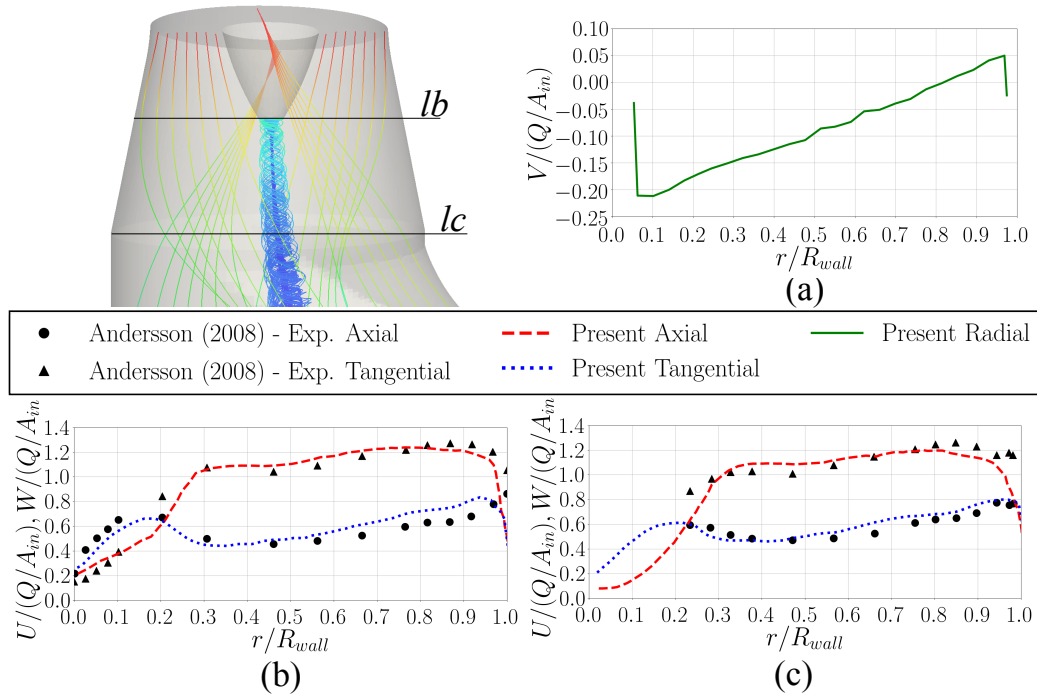


Figure 2: Comparison of the circumferentially averaged velocity components to experimental data from the literature at the two levels within the cone section; (a) Radial velocity at  $lc$  level; (b) Axial and tangential components at  $lb$  level; (c) Axial and tangential components at  $lc$  level. The CFD profiles were derived from a steady-state simulation with grid resolution ‘Mesh B’ outlined in §2.3.

201 Fig.2 shows the circumferentially-averaged velocity components at two



202 levels of the inflow cone. The velocity components are normalised by the  
 203 volumetric discharge at the inflow boundary. For comparison, the equivalent  
 204 phase-averaged LDA measurements by Andersson and Cervantes [26] have  
 205 also been plotted. It can be seen in this figure that the inflow methodology  
 206 described above validates well with the equivalent experimental setup.

## 207 2.2. Draft tube performance measures

208 The main function of the draft tube is to recover kinetic energy from the  
 209 turbine runner by increasing the pressure head. A typical measure of this  
 210 conversion is given by the pressure recovery factor,

$$C_p = \frac{1}{\frac{1}{2}\rho \left(\frac{Q}{A_{in}}\right)^2} \left[ \frac{1}{A_{out}} \int_{A_{out}} \bar{p}_{out} dA_{out} - \frac{1}{A_{in}} \int_{A_{in}} \bar{p}_{in} dA_{in} \right], \quad (10)$$

211 where  $A$  denotes the cross-sectional area for the inflow (*in*) and outflow (*out*)  
 212 boundaries respectively. Maximising  $C_p$  is the primary objective in draft tube  
 213 design. Conversely, another performance indicator,  $\zeta$ , expresses the energy  
 214 that is converted to a form that can not be used during the operation of  
 215 an energy producing, consuming, or conducting system (e.g. that due to  
 216 frictional losses). Typically,  $\zeta$  is defined [28]:

$$\zeta_1 = \frac{1}{\frac{1}{2}\rho \left(\frac{Q}{A_{in}}\right)^2} \left[ \frac{1}{A_{in}} \int_{in} P_{t,in} dA_{in} - \frac{1}{A_{out}} \int_{out} P_{t,out} dA_{out} \right], \quad (11)$$

217 where  $P_t$  is the total pressure, i.e.,  $P_t = \bar{p} + 0.5\rho(U_i^2)$ . Alternatively, the  
 218 energy loss of the draft tube has been expressed in the literature in other  
 219 forms [26]:

$$\zeta_2 = \frac{1}{\frac{1}{2}\rho \left(\frac{Q}{A_{in}}\right)^2 U_i \cdot n} \left[ \frac{1}{A_{in}} \int_{in} P_{t,in} U_i \cdot n dA_{in} + \frac{1}{A_{out}} \int_{out} P_{t,out} U_i \cdot n dA_{out} \right], \quad (12)$$

220 where  $\cdot n$  indicates the component normal to the corresponding boundary – it  
 221 should be noted that this component is negative at the inflow. The pressure  
 222 recovery coefficient has also been reported in other forms [26]:

$$C'_p = \frac{1}{\frac{1}{2}\rho \left(\frac{Q}{A_{in}}\right)^2 U_i \cdot n} \left[ \frac{1}{A_{out}} \int_{A_{out}} \bar{p}_{out} U_i \cdot n dA_{out} - \frac{1}{A_{in}} \int_{A_{in}} \bar{p}_{in} U_i \cdot n dA_{in} \right], \quad (13)$$

223 which, to the best of the authors' knowledge, has not yet been quantified in  
 224 the literature. In this work,  $C_p$ ,  $\zeta_1$ , and  $\zeta_2$  will be used for validation of the  
 225 proposed CFD methodology in §2.4;  $C'_p$  on the other hand will be quantified  
 226 to serve as benchmark data.

227 *2.3. Grid regeneration methodology*

228 The automated meshing utility *cfMesh* [29] was used to generate the  
 229 CFD grid for each draft tube design. To construct the grid, *cfMesh* requires  
 230 a closed manifold-surface – typically a stereolithography file. From this, a  
 231 uniform hexahedral grid is generated within the enclosed surface. The inter-  
 232 nal grid is subsequently projected onto the manifold surface and a boundary  
 233 layer grid is constructed towards the interior using a set of user-defined pa-  
 234 rameters. *cfMesh* also provides additional controls for the boundary layer  
 235 quality, intended for situations where a large number of layers is required, or  
 236 where the thickness is needed to vary smoothly – the majority of these pa-  
 237 rameters were kept as default. The chosen regions for local refinement were  
 238 in the vicinity of the draft tube walls, inflow boundary, and the runner hub.  
 239 Fig.3 demonstrates 3 of the 9 key steps towards generating a predominately  
 240 hexahedral grid ( $\sim 95\%$ ), with occasional general polyhedral cells ( $\sim 5\%$ ) in  
 241 cumbersome regions of the domain.

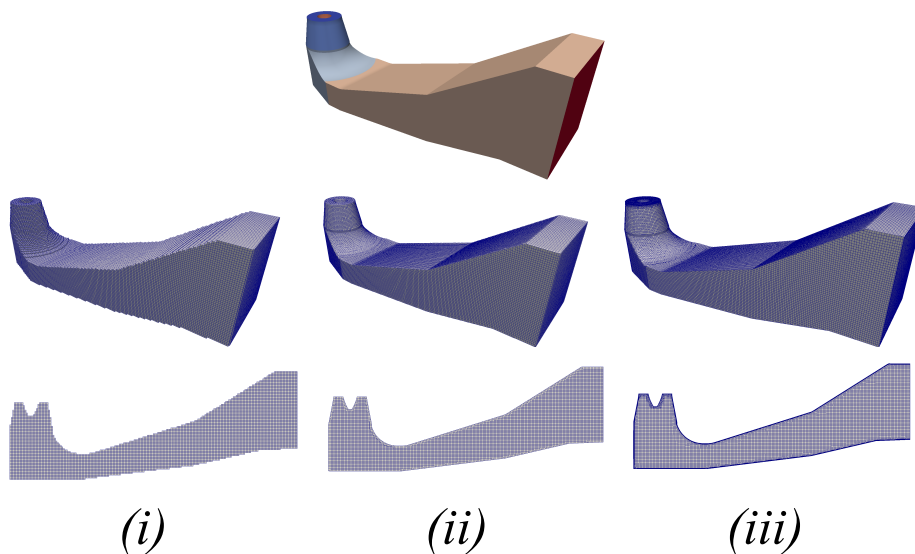


Figure 3: (Top) CAD geometry of the draft tube; (i) a uniform-hexahedral grid filling the internal domain; (ii) surface-projection of the internal grid onto the surrounding geometry; (iii) near-wall grid untanglement, boundary-layer construction and local region refinement.

242 By experimentation, the most influential parameters needed for a grid  
 243 independency study was reduced to a set of 3:

- 244 • *maxCellSize*: defines the maximum cell size generated in the internal  
 245 grid;
- 246 • *localRefinement*: prescribes the surface cell size on a specified bound-  
 247 ary;
- 248 • *maxFirstLayerThickness*: prescribes the first wall-normal cell height to  
 249 a specified boundary.

250 Four grids are generated varying the above parameters. The correspond-  
 251 ing settings are shown in Table 3. ‘Mesh A’ has the coarsest resolution with  
 252 the first cell height from the draft tube walls varying between  $53 \leq y_1^+ \leq 287$   
 253 (where  $y_1^+ = y_1 u_\tau / (\nu + \nu_t)$ ,  $y_1$  is the cell-center height, and  $u_\tau$  is the shear  
 254 velocity). ‘Mesh B’ has a smaller maximum cell-size, refinement, and first-  
 255 layer boundary layer thickness than ‘Mesh A’ – the near-wall resolution was  
 256 reduced to  $33 \leq y_1^+ \leq 187$ . ‘Mesh C’ has the same maximum cell-size as  
 257 ‘Mesh B’, and the same near-wall resolution as ‘Mesh A’. Finally, ‘Mesh D’  
 258 increases the mesh resolution within the domain and has the same near-wall  
 259 resolution as ‘Mesh B’.

	Refinement		Boundary-layer	
Mesh	maxCellSize	localRefinement	maxFirstLayerThickness	Total no. cells
A	0.02	0.025	0.035	1055311
B	0.015	0.0125	0.0175	2220036
C	0.015	0.0125	0.035	4280803
D	0.0075	0.005	0.0175	8491178

Table 3: User-defined parameters used in cfMesh and resulting total number of cells for each CFD grid.

260 Steady-state simulations using the numerical setup described in §2.1 were  
 261 performed on the four grids. For comparison, a time-averaged transient sim-  
 262 ulation was performed on ‘Mesh B’. The steady-state simulations were con-  
 263 sidered converged when the residuals for the flowfield variables descended  
 264 below  $10^{-6}$ . For the unsteady simulation, the flowfield quantities were time-  
 265 averaged over a nondimensional time-period of  $t^* = t(Q/A_{in})/L = 25$  ( $L$  is

266 the length of the draft tube in the  $x$ -direction) with satisfactory convergence  
 267 of the statistics. Fig.4 shows the profiles of the normalised wall pressure  
 268 coefficient along the upper and lower walls along the centerline:

$$C_{pw} = \frac{\bar{p}_{wall} - \bar{p}_{in,wall}}{\frac{1}{2}\rho \left(\frac{Q}{A_{in}}\right)^2}, \quad (14)$$

269 where  $\bar{p}_{wall}$  is the local static pressure on the wall. For comparison, the  
 270 experimental measurements by Andersson and Cervantes [26] and Čarija et  
 271 al. [21] are also plotted along side the present results. It can be seen that the  
 272 present results are consistent with the experimental data in the inflow cone  
 273 region. Downstream, a large disparity can be seen around the heel section,  
 274 especially along the lower wall, where attaining an accurate measurement  
 275 for pressure is troublesome for both experimental and numerical approaches;  
 276 for the former, this is demonstrated through the disparity of experimental  
 277 measurements between Andersson and Čarija et al., for the latter, the in-  
 278 ability of CFD to validate in the corner region has been recorded for more  
 279 advanced turbulence modelling approaches such as Detached-Eddy Simula-  
 280 tion [30]. Finally, along the diffuser section, the present and experimental  
 281 results return to a close agreement for both the upper and lower walls. Over-  
 282 all, although there is some deviation in the elbow section, the present results  
 283 clearly agree the trend of the experimental measurements, and the CFD re-  
 284 sults show a consistent profile regardless of the cfMesh parameters pertaining  
 285 to the near-wall resolution.

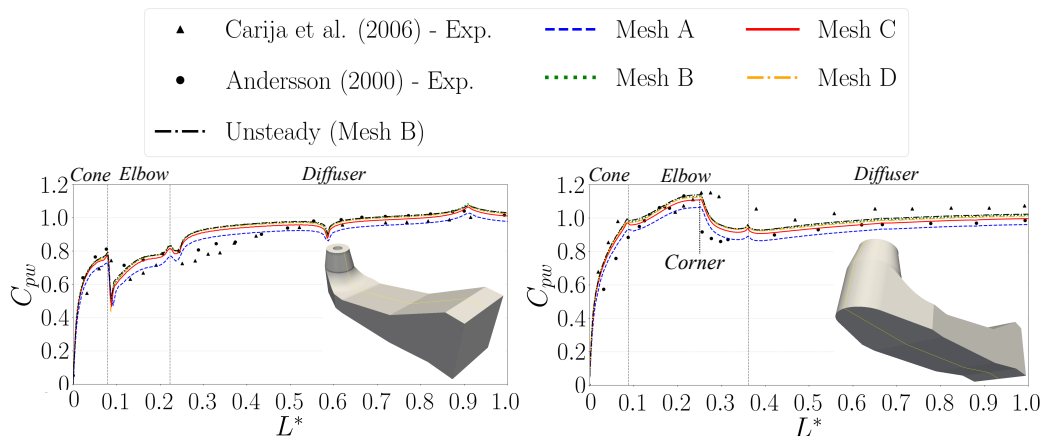


Figure 4:  $C_{pw}$  (Eq.14) distributions along the upper and lower wall centerlines using the cfMesh parameters shown in Table 3, Steady-state and time-averaged unsteady simulations.  $L^*$  is the normalised length of the lower and upper walls along the centerline (-).

286 Of the grids considered, ‘Mesh A’, with the coarsest grid, showed the poor-  
 287 est consistency to the other grid resolutions around the lower floor of the heel  
 288 section. This can be largely attributed to the limitations of the turbulence  
 289 modelling in the near-wall region or lack of flow physics from the mesh reso-  
 290 lution in the freestream. Čarija et al. [21] had previously demonstrated that  
 291 the choice of turbulence model had little effect on the wall pressure, but did  
 292 comment on the sensitivity of the near-wall resolution. Despite this result,  
 293 the minimum number of cells required to adequately capture the complex flow  
 294 along the draft tube walls (especially separation) was for ‘Mesh B’ or ‘Mesh  
 295 D’. Furthermore, to maintain a near-wall resolution range of  $30 < y_1^+ < 300$   
 296 for the first-cell height from the walls, required for the  $k - \epsilon$  models, the  
 297 boundary-layer parameters from ‘Mesh B’ or ‘Mesh D’ are required. Finally,  
 298 it can also be observed that there is little deviation between the steady-state  
 299 and unsteady (time-averaged) simulations.

#### 300 2.4. Validation of CFD modelling

301 Table 4 shows the calculated performance quantities outlined in §2.2 for  
 302 different grid resolutions and those obtained from the literature. It can be  
 303 seen that the present results largely agree with the equivalent CFD studies  
 304 - especially those from the more recent papers ([6, 7, 28, 8]), which use a  
 305 similar CFD setup to the present work. However, the benchmark experimen-  
 306 tal results for pressure recovery from the 2nd Turbine-99 Workshop [14] is  
 307 generally larger than the CFD results. This observation is unsurprising, as  
 308  $C_p$  is attained through an area-weighted averaging over the cross-section and  
 309 is therefore more difficult to determine experimentally. For the experimen-  
 310 tal approximation of pressure recovery,  $C_p$  (Exp.), the mean pressure at the  
 311 outflow was estimated from the wall pressure,  $p_{out,wall}$ , since the pressure can  
 312 only be measured in this vicinity at the outflow section [14]. The method of  
 313 calculating  $C_p$  (Exp.) has been replicated in the present CFD calculations,  
 314 based on probe locations specified in the 2nd Turbine-99 workshop [14]. A  
 315 distinctive 3 – 4% increase in pressure recovery is attained over the equiva-  
 316 lent area-weighted results. Quantification of the alternate pressure recovery  
 317  $C'_p$  demonstrates that this is more sensitive to the grid resolution than the  
 318 conventional  $C_p$ , due to the fluctuating velocity distribution at the sample  
 319 plane.

320 Like  $C_p$ ,  $\zeta$  requires the measurement the flowfield over the inflow and out-  
 321 flow cross-sections and is seldom quantified in experimental work. However,  
 322 for CFD it is easily determined. It can be seen in Table 4 that the validation

323 of  $\zeta$  becomes difficult due to the limited number of sources. The summary  
 324 of CFD results from the Turbine-99 Workshops [17, 14, 18] shows a scatter  
 325 of values for  $\zeta_2$  in which the present results fall within this range. It can also  
 326 be seen in Table 4, for the present work, the values  $\zeta_1$  and  $\zeta_2$  increase with  
 327 number of cells, while the values of  $C_p$  decrease to a converged result.

Case	$C_p$ (Eq.10)	$C'_p$ (Eq.13)	$C_p$ (Exp.)	$\zeta_1$ (Eq.11)	$\zeta_2$ (Eq.12)
Mesh A	0.9641	0.9655	0.9836	0.1375	0.1562
Mesh B	0.9563	0.9586	0.9890	0.1445	0.1630
Mesh C	0.9563	0.9580	0.9908	0.1463	0.1645
Mesh D	0.9562	0.9571	0.9820	0.1465	0.1647
Mesh B (unsteady)	0.9566	0.9559	0.9895	0.1447	0.1658
[14] Exp.	[-]	[-]	1.02 – 1.1	[-]	0.09 ± 0.06
[26] CFD (summary)	0.887 – 0.991	[-]	[-]	[-]	0.066 – 0.172
[18] CFD (summary)	0.710 – 1.032	[-]	[-]	[-]	0.043 – 0.301
[6] CFD (steady, $k - \epsilon$ )	0.9573	[-]	[-]	[-]	0.0790
[7] CFD (steady, $k - \epsilon$ )	0.9588	[-]	[-]	[-]	[-]
[7] CFD (unsteady, $k - \epsilon$ )	0.9588	[-]	[-]	[-]	[-]
[8] CFD (steady, $k - \epsilon$ )	0.8855	[-]	[-]	0.1755	[-]

Table 4: Performance quantities obtained from the present grids, and those obtained from the literature.  $C_p$  (Exp.) calculates the pressure at the inflow and outflow boundaries based on probe locations specified by the 2nd Turbine-99 workshop [14].

328 It is also interesting to observe the development of performance quantities  
 329 along the draft tube. A series of sample planes are placed along the draft tube  
 330 in the positions indicated in Fig.5(top). The performance quantities were  
 331 calculated on these planes using Eqs.10 and 12, where *out* is synonymous  
 332 with the position of the plane (e.g.,  $p_{out} = p_A$  at position *A*). Fig.5(bottom)  
 333 shows the development of the performance quantities along the draft tube  
 334 for different grid resolutions. The  $C_p$  progression conforms the observation  
 335 above for its insensitivity to the grid resolution and use of steady/unsteady  
 336 simulations. Furthermore, it can also be seen that the pressure recovery  
 337 is largest within the inflow cone and heel regions.  $\zeta$  on the other hand  
 338 is considerably more sensitive to the grid resolutions than  $C_p$ , but appears  
 339 insensitive to the use of steady/unsteady simulations.

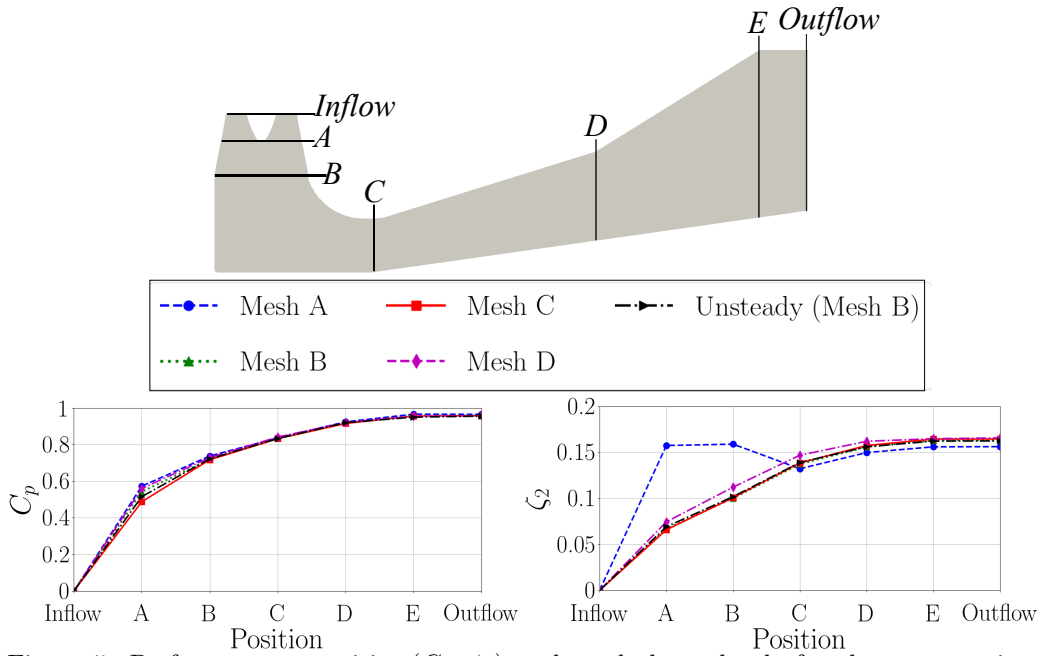


Figure 5: Performance quantities ( $C_p$ ,  $\zeta_2$ ) evaluated along the draft tube cross-sections for various mesh resolutions.

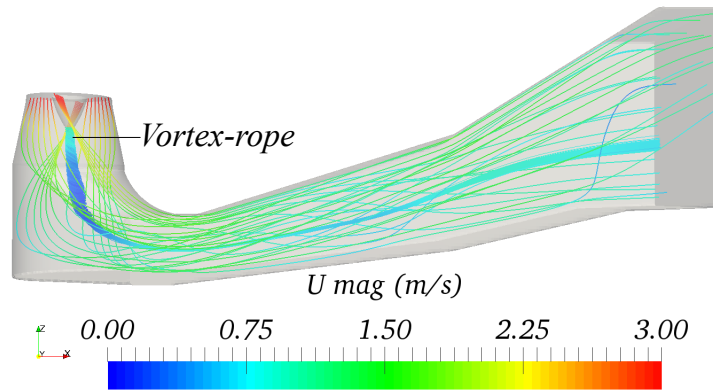


Figure 6: Streamlines of the flow along the base draft tube design.

340 Fig.6 shows the velocity streamlines along the draft tube geometry from  
 341 the present work. Despite the disparity of reported pressure recovery, the  
 342 vortex-rope formation is similar to those previously reported in equivalent  
 343 CFD studies (e.g., [6, 21]) but not in experimental observations [31]. Con-  
 344 sidering the present CFD setup, there are three possible explanations for the  
 345 differences to the experimental results:

- 346 1. the flow through the draft tube is assumed to be at a steady-state, even  
347 though it clearly poses transient characteristics, leaving many of the  
348 impressionable flow features (i.e. extent of flow separation) absent;
- 349 2. the limitations of RANS modelling: in theory, increasing the fidelity of  
350 the turbulence modelling approach would result in a closer simulated  
351 flowfield to the equivalent experiments. However, according to the  
352 participants of the 2nd Turbine-99 Workshop [14], it is debated whether  
353 the standard  $k-\epsilon$  model is capable of predicting the major flow features  
354 of the base case and performance quantities [17, 14];
- 355 3. the assumptions made in simulating the discharge from a Kaplan tur-  
356 bine. These are threefold: the reliability of the symmetrical axial, ra-  
357 dial, and tangential velocity profiles suggested in the Turbine-99 work-  
358 shops. Regarding the first assumption, the axial velocity profile is  
359 unlikely to be symmetric [32], forming a ‘Rotating Vortex-Rope’ below  
360 the runner, as observed in experiments [26]. Secondly, the radial veloc-  
361 ity has a significant influence on the vortex-rope formation and draft  
362 tube efficiency [33]. The boundary condition for the radial velocity  
363 (Eqs.6-7) serves as an intuitive approximation. Finally, the tangential  
364 velocity requires a very fine grid resolution near the wall of the runner  
365 as the profile alternates in sign (large velocity gradient) in this region.  
366 This change of sign originates from the log-wall assumption and the  
367 fitting of measured tangential velocity profile [26], whose accuracy is  
368 questionable [20].

369 It is suggested that despite the limitations described above, the present  
370 CFD methodology provides a suitable approximation of the flowfield and  
371 draft tube performance values. The quantified wall pressures and perfor-  
372 mance quantities carried out in this section support this conclusion.

### 373 2.5. Verification of numerical errors

374 In this section, the method for estimating the uncertainty of CFD solu-  
375 tion due to the resolution of the grid is outlined.  
376 Grid independency analysis was conducted through the GCI (Grid Conver-  
377 gence Index) method [12], which has previously been employed for draft tube  
378 flows [34]. The representative cell size  $h_i$  for each grid  $i$  is described

$$h_i = \left[ \frac{1}{N_i} \sum_{j=1}^{N_i} (\Delta V_j) \right]^{1/3}, \quad (15)$$



379 where  $N_i$  is the number of cells, and  $V_j$  is the volume of each cell  $j$ . As  
380 observed in §2.4, ‘Mesh A’ was unable to produce physically meaningful  
381 results due to the low resolution of the internal domain and near-wall regions.  
382 Therefore, grid resolutions ‘Meshes B-D’ outlined in §2.3 were chosen for  
383 this analysis. The maximum non-orthogonality for the finest grid (‘Mesh  
384 D’) was approximately  $60^\circ$ , while the average value is approximately  $7^\circ$ .  
385 The resulting grid refinement factor ( $h_{coarse}/h_{fine}$ ) is 3.825 – larger than the  
386 minimum recommended 1.3 [12]. The three grids are ranked  $h_1 < h_2 < h_3$ .  
387 The apparent order of grid convergence,  $\alpha$ , is determined through a fixed-  
388 point iteration of the expression:

$$\alpha = \frac{1}{\ln(h_2/h_1)} \left| \ln \left| \frac{\phi_3 - \phi_2}{\phi_2 - \phi_1} \right| + \ln \left( \frac{(h_2/h_1)^\alpha - 1 \cdot \operatorname{sgn} \left( \frac{\phi_3 - \phi_2}{\phi_2 - \phi_1} \right)}{(h_3/h_2)^\alpha - 1 \cdot \operatorname{sgn} \left( \frac{\phi_3 - \phi_2}{\phi_2 - \phi_1} \right)} \right) \right|, \quad (16)$$

389 where  $\phi$  is the performance quantity under consideration. Hence, an extrap-  
390 olated value for the performance quantity  $\phi$  can be obtained using

$$\phi_{ext}^{21} = \frac{(h_2/h_1)^\alpha \phi_1 - \phi_2}{(h_2/h_1)^\alpha - 1} \quad (17)$$

391 and the grid uncertainty estimations are determined:

392 Approximate relative error,

$$e_a^{21}(\%) = 100 \cdot \left| \frac{\phi_1 - \phi_2}{\phi_1} \right|; \quad (18)$$

393 extrapolated relative error,

$$e_{ext}^{21}(\%) = 100 \cdot \left| \frac{\phi_{ext}^{21} - \phi_1}{\phi_{ext}^{21}} \right|; \quad (19)$$

394 fine-grid convergence index,

$$GCI_{fine}^{21}(\%) = 100 \cdot \left( \frac{1.25e_a^{21}}{(h_2/h_1)^\alpha - 1} \right). \quad (20)$$

395 The pressure recovery factor (Eq.10) was used to assess the grid uncertainty.  
396 It should be noted this is estimated through an area-weighted process – re-  
397 ducing the sensitivity to the grid. To demonstrate this aspect, an arithmetic

398 average of the pressure recovery is performed over the faces of each sample  
 399 plane (see Fig.5(top)):

$$C_p \left( \sum \right) = \frac{\frac{\sum_{j=1}^{N_{out}} p_{out}}{N_{out}} - \frac{\sum_{j=1}^{N_{in}} p_{in}}{N_{in}}}{\frac{1}{2} \rho \left( \frac{Q}{A_{in}} \right)^2}. \quad (21)$$

400 Using this definition, the GCI results are shown in Table 5. It can be seen  
 401 that the apparent order of convergence is limited to the order of the numer-  
 402 ical method (2nd). Naturally, some numerical diffusion is expected, with  
 403 the estimation being suitably larger than 1 [12] for all cross-sections along  
 404 the draft tube. Moreover, the estimated uncertainty reduces monotonically  
 405 along the draft tube - regardless of the local flowfield features. The largest  
 406 uncertainty is 4.76% at the base of the runner hub, which is still sufficient  
 407 for interpretation (< 10% [12]).

$\phi$	Plane	$\alpha$	$\phi_{ext}^{21}$	$e_a^{21}$ (%)	$e_{ext}^{21}$ (%)	$GCI_{fine}^{21}$ (%)
$C_p$ ( $\sum$ )	A	1.2235	0.3071	-1.9214	-4.3118	-4.7660
	B	1.3129	0.6274	-1.8089	-1.8354	-1.9385
	C	1.5317	0.8264	-0.8236	-1.2972	-1.6010
	D	1.6439	0.8929	-0.6633	-1.2289	-1.2797
	E	1.7604	0.9561	-0.7958	-0.7758	-0.9623
	Outflow	1.8814	0.9569	-0.6191	-0.3188	-0.3973

Table 5: GCI results for the un-weighted averaging for the pressure recovery (Eq.21) at sample planes along the base geometry (see Fig.5(top)).

408 Table 6 shows the GCI results for the area-weighted estimation of the  
 409 pressure recovery (Eq.10). It can be seen that this representation shows  
 410 a greater independence to the grid resolution than the arithmetic estima-  
 411 tion (Eq.21). At the same time, it can be seen that the apparent order of  
 412 convergence (and corresponding uncertainty) now fluctuates with the local  
 413 cross-sectional area of the sample plane. It should be noted that the val-  
 414 ues of extrapolated pressure recovery are similar regardless of the estimation  
 415 method.

$\phi$	Position	$\alpha$	$\phi_{ext}^{21}$	$e_a^{21}$ (%)	$e_{ext}^{21}$ (%)	$GCI_{fine}^{21}$ (%)
$C_p$	A	2.5424	0.5319	-0.4539	-0.5803	-0.7212
	B	2.1475	0.7349	-0.1050	-0.1662	-0.2074
	C	5.7901	0.8380	-0.0086	-0.0031	-0.0039
	D	4.4686	0.9231	-0.0869	-0.0490	-0.0612
	E	3.8923	0.9563	-0.1761	-0.1232	-0.1538
	Outflow	3.3593	0.9562	-0.3801	-0.3312	-0.4178

Table 6: GCI results for the area-weighted averaging for the pressure recovery (Eq.10) at sample planes along the base geometry (see Fig.5(top)).

### 416 3. Draft tube design study

417 In this section, the CFD methodology described in §2.1 is used to evaluate  
418 proposed design recommendations for the draft tube in the literature. The  
419 focus of this analysis will be on the inflow cone and outer-heel, as the greatest  
420 pressure recovery occurs these regions. The automatic construction of the  
421 closed-manifold surfaces was achieved using Glyph scripting (using TCL)  
422 in Pointwise R18.2. These were imported to cfMesh which automatically  
423 generated the CFD grid for each draft tube design (described in §2.3).

#### 424 3.1. Inflow cone section

425 As seen in Fig.5, the greatest recovery of pressure occurs in the inflow  
426 cone, due to flow separation below the runner hub. This phenomenon is  
427 controlled to some extent by the runner hub design (diameter, length, and  
428 shape of bulb). While altering the shape of the runner hub is not considered  
429 in this research, the same effect can be achieved by altering the cross-sectional  
430 area surrounding this component [6, 35]. Convex and concave inflow cone  
431 designs are considered in the present work, along with the optimum design  
432 from 2nd part of this research [36] – which has a slighter larger radius than  
433 the base geometry.

434 To alter the inflow cone radius, a single control point is positioned at the  
435 lowest level of the hub. The side of the inflow cone was represented by a  
436 single Catmull-Rom spline [37] — possessing  $C^1$  parametric continuity. The  
437 spline implementation is indicated in Fig.8(a). The considered radii of the  
438 inflow cones were  $r = 0.3m$ ,  $0.205m$ , and  $0.5m$  (base design,  $0.28m$ ) – the  
439 last two cases are shown in Fig.8(b) and (c).

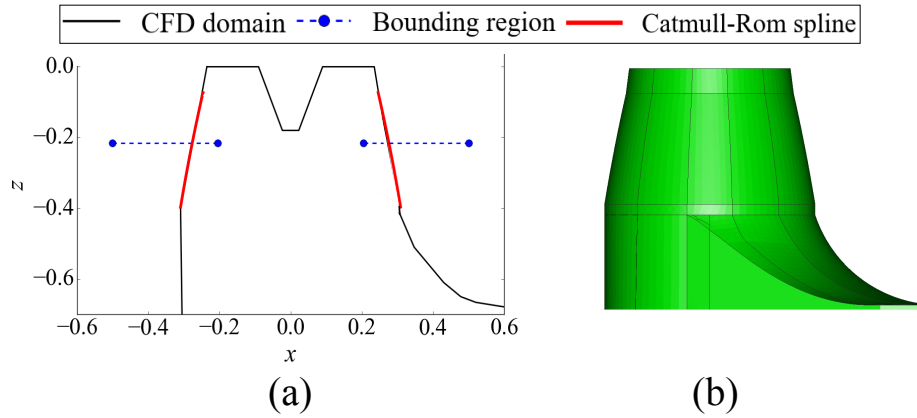


Figure 7: A demonstration of the inflow cone radius bounds considered in this work; (a) a schematic of the inflow cone with the bounds for the control point; (b) the base design. All dimensions are in *cm*.

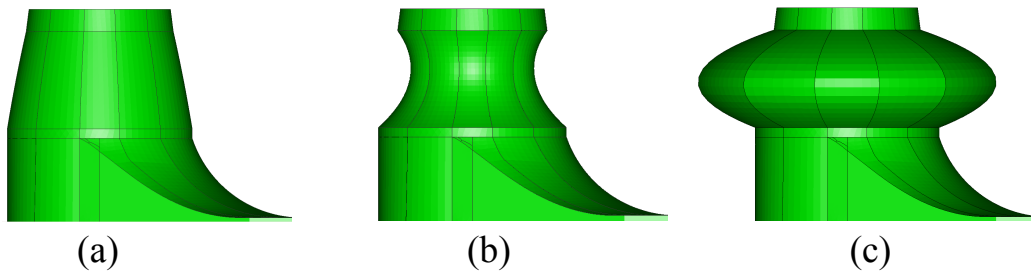


Figure 8: A demonstration of the inflow cone geometries considered investigation; (a) the base design; (c) the smallest radius considered; (d) the largest radius considered.

440 Fig.9 shows the velocity streamlines through the draft tube with different  
 441 inflow cone radii. It can be seen that the vortex-rope dissipates (along with  
 442 the swirl intensity) as the area around the runner hub is reduced. For the  
 443 convex design, the effective vortex cavities cause the flow to separate along  
 444 the inflow cone walls, though the vortex rope is largely left unaffected by  
 445 this effect. This trend confirms the speculations made by several authors  
 446 [1, 26, 35, 38].

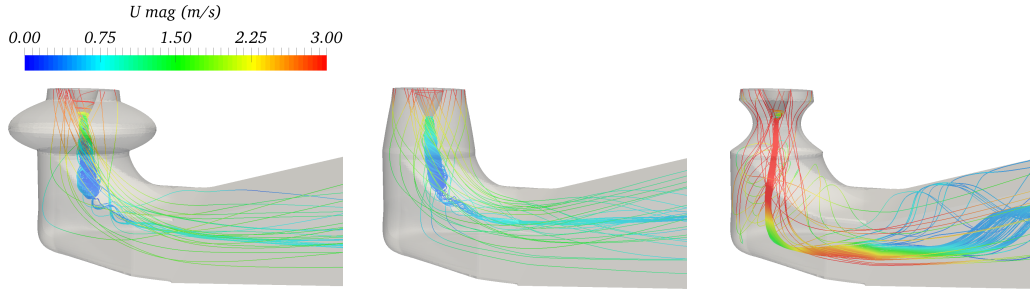


Figure 9: Streamlines along the draft tube with various inflow cone designs (with base heel and diffuser).

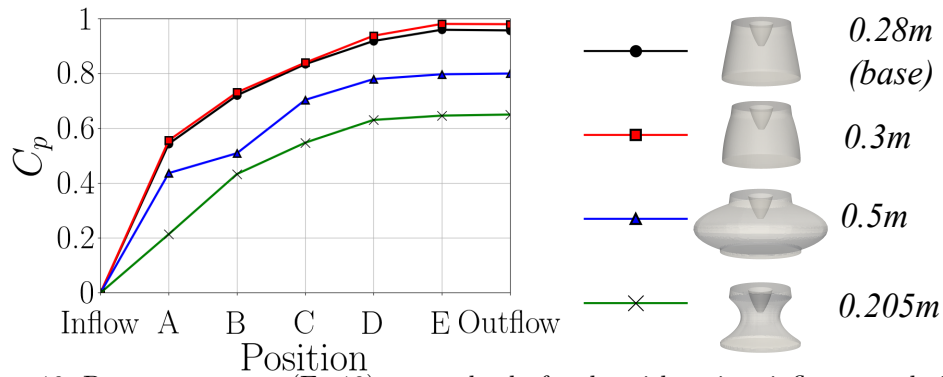


Figure 10: Pressure recovery (Eq.10) across the draft tube with various inflow cone designs.

447 Fig.10 shows the progression of pressure recovery along the draft tube for  
 448 various inflow cone designs. The location of the sample planes are indicated  
 449 in Fig.5(top). From Fig.10, a number of trends can be observed:

- 450 • the pressure recovery along the heel and diffuser sections are scaled  
 451 according to the pressure recovery around the inflow cone (sample-  
 452 plane ‘A’);
- 453 • The extreme designs of large and small cone radii have a detrimental  
 454 effect to the overall pressure recovery;
- 455 • For the large cone radius, the pressure recovery reduced around the  
 456 base of the cone (sample-plane ‘B’).

457 Overall, it is shown in this section that the design of the inflow cone signifi-  
 458 cantly affects the vortex-ropes and resulting efficiency of the draft tube. GCI

459 analysis (see §2.5) is also applied to the draft tube designs. Input parameters  
 460 for ‘Meshes B-D’ (§2.3) were used to generate the grids while the pressure  
 461 recovery factor (Eq.10) was used to assess the grid uncertainty. The results  
 462 of this analysis are shown in Table 7, with the apparent trends:

- 463 • inflow cone with radius 0.3m has similar results to the base design  
 464 (Table 6);
- 465 • reducing the radius of the inflow cone increases the error significantly,  
 466 with no apparent relation to the local cross-sectional areas;
- 467 • the inflow cone with the largest radius has a similar pattern to the base  
 468 design but with larger errors.

Inflow cone	Plane	$\alpha$	$\phi_{ext}^{21}$	$e_a^{21}$ (%)	$e_{ext}^{21}$ (%)	$GCI_{fine}^{21}$ (%)
0.205m	A	5.4742	0.2130	-1.2257	-0.3222	-0.4014
	B	2.7336	0.4105	-0.6188	-0.5474	-0.6487
	C	5.1024	0.5263	-0.5464	-3.9515	-0.4752
	D	2.1918	0.6241	-0.8178	-0.9418	-0.1166
	E	3.2586	0.6237	-0.5270	-0.3521	-0.4252
	Outflow	4.6411	0.6482	-0.1270	-0.2220	-0.2769
0.3m	A	2.7268	0.5540	-4.5258	-3.9564	-4.7572
	B	2.7812	0.7390	-0.3023	-0.2477	-0.3088
	C	5.0627	0.8382	-0.2432	-0.0741	-0.0926
	D	4.6212	0.9357	-0.3263	-0.1178	-0.1471
	E	3.6197	0.9776	-0.3351	-0.1835	-0.2290
	Outflow	2.8871	0.9763	-0.3275	-0.2540	-0.3167
0.5m	A	1.4943	0.3938	-2.8463	-5.6171	-6.6480
	B	2.0309	0.4924	-2.2497	-1.0436	-1.2910
	C	4.6430	0.7323	1.4614	0.5213	0.6551
	D	2.4561	0.8021	1.3459	1.2986	1.6446
	E	1.9325	0.8340	1.4648	1.9388	2.4714
	Outflow	1.3050	0.8297	1.0744	2.3114	2.9577

Table 7: GCI results for the area-weighted averaging for the pressure recovery (Eq.10) at sample planes (see Fig.5) along geometries with different inflow cone radii.

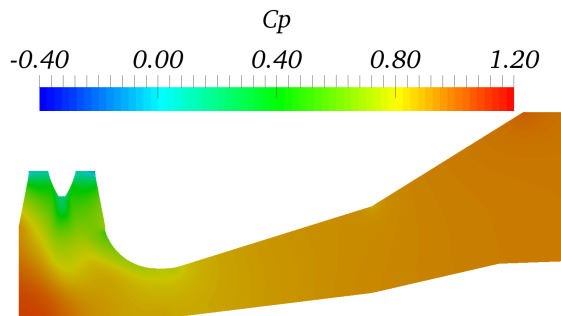


Figure 11: Pressure recovery (Eq.10) contour down the centerline for base design.

470 The sharp-heel construction of the base design is a rather unusual choice  
 471 from the perspective of the fluid flow. Indeed, the presence of a sharp-heel  
 472 is reported to contribute an efficiency loss ( $C_p$ ) of approximately 0.3-2.3%  
 473 [1]. As seen in Fig.11, a significant variation of pressure can be seen in  
 474 the elbow as the flow is redirected from the inflow cone to the diffuser. The  
 475 stagnation region creates a diversion of the flow to the outer-wall of the elbow,  
 476 forming a non-uniform velocity distribution at the opening of the diffuser  
 477 section. At the same time, the sudden changes in cross-sectional area along  
 478 the elbow incurs large regions of flow separation, reducing the draft tube  
 479 efficiency. Based on these characteristics, the draft tube can be improved by  
 480 maintaining or reducing the cross-sectional areas across the elbow section, or  
 481 by incorporating design features which mitigate flow separation.

482 Along with the base (sharp-heel) design, this section will analyse the draft  
 483 tube with the following outer-heel designs:

- 484 1. curved-heel proposed by Dahlbäck [39];
- 485 2. expanded-heel (*vortex-chamber*) inspired by [40, 41, 42];
- 486 3. chamfered-heel proposed by Daniels et al. [36].

487 A flexible method was chosen to create the heel shapes described above. A  
 488 Catmull-Rom spline was implemented on the  $xz$ -center-plane on the outer-  
 489 wall of the heel, as indicated in Fig.13a, which is subsequently projected  
 490 around the heel as indicated in Fig.13b. Fig.12 shows the schematic of the  
 491 Catmull-Rom spline implementation. The proposed representation is also  
 492 capable of recreating the original sharp-heel design.

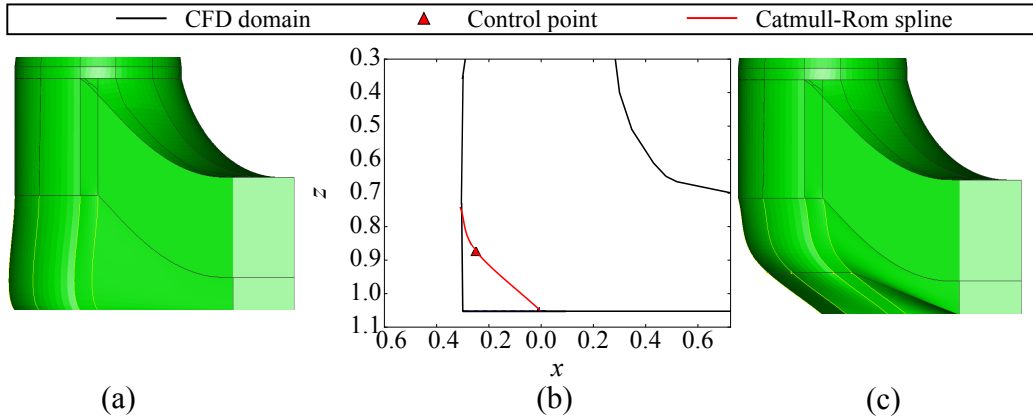


Figure 12: A demonstration of altering the heel design; (a) base heel construction using proposed heel representation; (b) schematic of the Catmull-Rom spline implementation, and control point; (c) a demonstration of the deformed heel using the spline formation in (b). All dimensions are in *cm*.

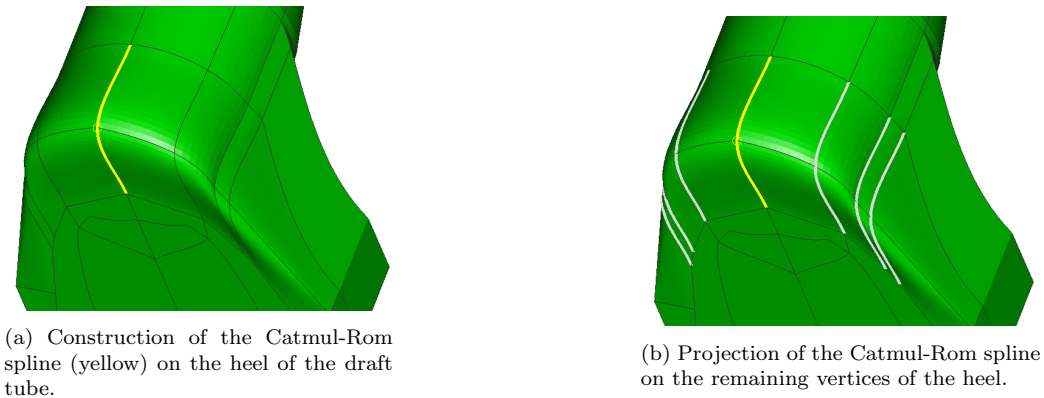


Figure 13: Implementation of the Catmull-Rom spline on the heel section.

493 Fig.14 shows the normalised pressure and velocity contours along the  $xz$ -  
 494 center-plane for the sharp, curved, chamfered, and expanded heel designs.  
 495 For the sharp-heel, the flowfield shows three separation regions: beneath  
 496 the runner cone, outer corner of the heel, and upper wall at the entrance  
 497 of the diffuser. When considering the curved-heel design, the recirculation  
 498 in the heel corner disappears, increasing the pressure recovery by 1.92% to  
 499 the sharp-heel design; this estimation is slightly larger than the experimen-  
 500 tal prediction of 1-1.5% [39]. A similar phenomenon can be seen for the  
 501 expanded-heel, with a 1% increase of pressure recovery to the sharp-heel de-  
 502 sign. Finally, for the chamfered heel, small separation regions are formed at



503 the top-left and bottom walls. The pressure recovery increases by 2.79% to  
 504 the sharp-heel design. Furthermore, it can be seen in Fig.14 that the pressure  
 505 flowfield around the inner-wall of the heel is largely insensitive to the  
 506 heel design. The noticeable difference between the draft tube designs can be  
 507 seen for the separation region below the runner hub. The velocity contours  
 508 show the recirculation in this region increases with the expansion of the heel.  
 509 Hence, a larger separation region beneath the runner hub is created reducing  
 510 the pressure recovery. Smoothing the sharp-heel corner with an curved (or  
 511 chamfered) heel reduces the swirl intensity of the flow and increases axial  
 512 velocity across the inflow cone and heel, which consequently increases the  
 513 draft tube efficiency.

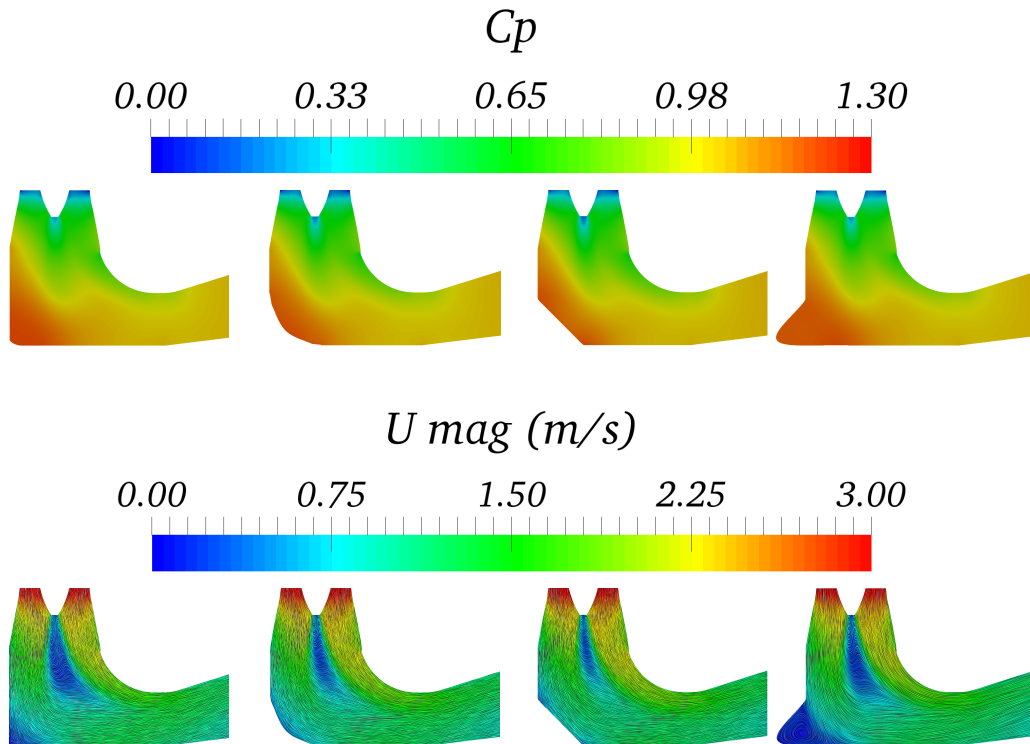


Figure 14: The normalised pressure distribution (top) and velocity magnitude (bottom) along the  $xz$ -center-plane through the draft tube. From left-to-right: base geometry, curved-heel [39], chamfered [36], and expanded heel design.

514 Fig.15 shows the pressure recovery across various sample-planes (see Fig.5(top))  
 515 along the draft tube for the various heel designs. It can be seen that regardless  
 516 of the heel design, the pressure recovery remains unperturbed in the inflow

517 cone and heel sections of the draft tube. The difference in pressure recovery  
 518 occurs in the diffuser section – downstream of the heel. Hence, it can be  
 519 deduced that the heel design has a significant effect on the separation region  
 520 below the runner hub, which, while the pressure field is relatively unchanged  
 521 in the inflow cone and heel section, affects the uniformity of the velocity at  
 522 the entrance of the diffuser section and pressure recovery downstream of the  
 523 heel.

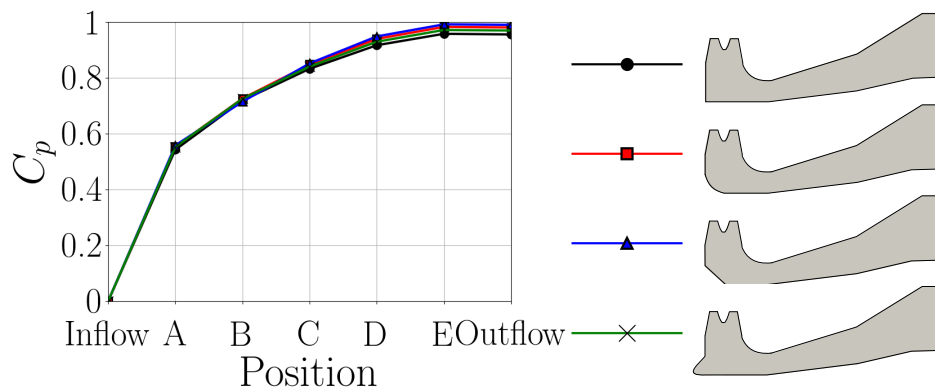


Figure 15: Pressure recovery across the draft tube with various heel designs.

524 Finally, GCI analysis (see §2.5) is applied to the draft tube designs. Input  
 525 parameters for ‘Meshes B-D’ (Table 3) were used to generate the grids in each  
 526 design, while the pressure recovery factor (Eq.10) was used to assess the grid  
 527 uncertainty. The results from this are shown in Table 8. Again, like the base  
 528 design, it can be seen that the uncertainty fluctuates with the local cross-  
 529 sectional area. At the same time, the grid uncertainty is considerably smaller  
 530 than the maximum allowed (<10% [12]) thus demonstrating the robustness  
 531 of the grid regeneration method and methodology for estimating the pressure  
 532 recovery.

Heel design	Plane	$\alpha$	$\phi_{ext}^{21}$	$e_a^{21}$ (%)	$e_{ext}^{21}$ (%)	$GCI_{fine}^{21}$ (%)
Curved	A	2.4108	0.5433	-0.0407	-0.0408	-0.0510
	B	2.0618	0.7315	-0.3570	-0.4449	-0.5536
	C	5.1458	0.8437	-0.1634	-0.0485	-0.0606
	D	3.4611	0.9347	-0.2233	-0.1318	-0.1645
	E	2.9682	0.9773	-0.2381	-0.1671	-0.2085
	Outflow	2.4595	0.9753	-0.2147	-0.2101	-0.2620
Expanded	A	2.3512	0.5451	-0.1761	-0.1867	-0.2291
	B	2.0485	0.7247	-0.1156	-0.1451	-0.1811
	C	5.6878	0.8375	-0.1463	-0.0357	-0.0446
	D	4.4210	0.9260	-0.1643	-0.0645	-0.0806
	E	3.6479	0.9675	-0.1839	-0.1012	-0.1264
	Outflow	3.2176	0.9661	-0.1643	-0.1792	-0.1514
Chamfered	A	2.6511	0.5441	-0.0983	-0.0866	-0.1081
	B	2.0793	0.7265	-0.1369	-0.1684	-0.2101
	C	5.1780	0.8486	-0.1653	-0.0403	-0.0503
	D	2.9135	0.9425	-0.2562	-0.1967	-0.2454
	E	2.8862	0.9858	-0.2443	-0.1902	-0.2373
	Outflow	2.4121	0.9840	-0.2395	-0.2409	-0.3004

Table 8: GCI results for the area-weighted averaging for the pressure recovery (Eq.10) at sample planes (see Fig.5) along geometries with different heel designs.

#### 533 4. Conclusions and future work

534 An investigation into the numerical modelling of a number of elbow-type  
535 draft tube designs was carried out, focusing on the grid sensitivity and per-  
536 formance of each design. To achieve this, Computational Fluid Dynamics  
537 (CFD) was used to evaluate the performance of the given draft tube design,  
538 while the open-source meshing software ‘*cfMesh*’ was used to automatically  
539 construct a predominately uniform hexahedral grid in each geometry.

540 A validation study of the numerical setup was undertaken on the sharp-  
541 heeled Hölleforsen-Kaplan draft tube (base design). From this it was con-  
542 cluded that the steady-state assumption validated well with the equivalent  
543 experimental data. Moreover, the sensitivity of the draft tube performance  
544 measures to the CFD grid shows that the energy loss factor,  $\zeta$ , is considerably  
545 more sensitive than the pressure recovery factor  $C_p$ . It was also found that

546 the estimation of pressure recovery through experimental measurements was  
547 consistently higher than the equivalent CFD method. The inflow cone and  
548 heel sections of the draft tube were identified as being the major contributing  
549 regions to the pressure recovery. Grid Convergence Index (GCI) analysis [12]  
550 was used to assess the uncertainty of pressure recovery related to the grid  
551 resolution. This was assessed at various cross-sections along the draft tube.  
552 From this two trends were identified:

- 553 1. estimating the pressure recovery by arithmetic averaging across the  
554 faces causes the apparent order of grid convergence to increase along  
555 the draft tube - limiting this to the order of numerical discretisation;
- 556 2. estimating the pressure recovery through area-weighted averaging caused  
557 the apparent order of grid convergence to fluctuate with the local cross-  
558 sectional area - the associated uncertainty is significantly reduced.

559 The 2nd part of this paper focuses on assessing the draft tube perfor-  
560 mance with different inflow cone and heel designs proposed in the literature.  
561 Specifically, this work considered:

- 562 • Varying the radius of the inflow cone from a concave to conex shape,  
563 including the optimum design identified in Part-2 of this research [36];
- 564 • Curved [39], chamfered [36], and expanded [40, 41, 42] outer-heel de-  
565 signs.

566 Catmull-Rom splines were used to achieve the above geometries. It was  
567 found that the optimum inflow design [36] improved the pressure recovery  
568 by 2.79% to the base geometry. Significantly reducing and expanding the  
569 inflow cone radius reduced the efficiency by 30.79% and 13.5% respectively.  
570 Furthermore, changing the outer-heel to a design other than a sharp-heel in-  
571 creased the pressure recovery, with improvements: chamfered - 2.79%, curved  
572 - 1.92%, and expanded - 1%. GCI analysis of the heel designs showed similar  
573 uncertainty values to the base design. On the other hand, for the various  
574 inflow cone designs, the apparent order of convergence for the concave de-  
575 sign broke down along with the vortex-rope. For all geometries considered  
576 in this work, the grid uncertainty was less than 10% (a limit specified by [12])  
577 demonstrating the robustness of the automated meshing software.

578 Overall, the novel aspects of this paper include:

- 579 • a proposed method for the automated reconstruction of the geometry  
580 and CFD grid for each evaluation;

- 581 • the characteristics of pressure recovery along the draft tube design  
582 through different methods of estimation;
- 583 • a study of the contributions of the inflow cone and heel components on  
584 the draft tube efficiency.

#### 585 *4.1. Future work*

586 This work naturally leads to the following topics of investigation on draft  
587 tube design:

- 588 1. additional design considerations such as the turbine design, and robust-  
589 ness of the draft tube performance;
- 590 2. design evaluation of the runner hub geometry — providing a greater  
591 potential for pressure recovery and geometric flexibility than the inflow  
592 cone.

#### 593 **Acknowledgments**

594 This work was supported by the UK Engineering and Physical Sciences  
595 Research Council [grant number EP/M017915/1]. The authors would also  
596 like to thank the helpful contributions of J. Angus, P. Burns, T. Dye, R.  
597 Gilbert, J. Gowans, S. Hardy, S. Hutchings and C. Ng. The CFD simulations  
598 were performed on the ISCA HPC in the Advanced Computing Facility in  
599 the University of Exeter, UK.

#### **References**

- [1] M. Gubin, Draft tubes of Hydro-electric Stations, Amerind Publishing Co., New Dehli, 1973.
- [2] B. Fabritius, G. Tabor, Improving the quality of finite volume meshes through genetic optimisation, *Eng. Comp.* 32 (3) (2016) 425–440. doi:10.1007/s00366-015-0423-0.
- [3] J. Samareh, Geometry and grid/mesh generation issues for CFD and CSM shape optimization, *Optimization and Engineering* 6 (1) (2005) 21–32. doi:10.1023/B:OPTE.0000048535.08259.a8.

- [4] T. Arispe, W. de Oliveira, R. Ramirez, Francis turbine draft tube parameterization and analysis of performance characteristics using CFD techniques, *Renew. Energy* 127 (2018) 114–124. doi:10.1016/j.renene.2018.04.055.
- [5] S. Daniels, A. Rahat, G. Tabor, J. Fieldsend, R. Everson, A review of shape distortion methods available in the openfoam framework for automated design optimisation, in: *OpenFOAM: Selected Papers of the 11th Workshop*, Springer International Publishing, 2019. doi:10.1007/978-3-319-60846-4\_28.
- [6] B. D. Marjavaara, T. S. Lundström, Redesign of a sharp heel draft tube by a validated CFD-optimization, *Int. J. Numer. Methods Fluids* 50 (8) (2006) 911–924. doi:10.1002/flid.1085.
- [7] J. Hellström, B. Marjavaara, T. Lundström, Parallel CFD simulations of an original and redesigned hydraulic turbine draft tube, *Adv. Eng. Softw.* 38 (5) (2007) 338–344. doi:10.1016/j.advengsoft.2006.08.013.
- [8] S. Galván, C. Rubio, J. Pacheco, S. Gildardo, C. Georgina, Optimization methodology assessment for the inlet velocity profile of a hydraulic turbine draft tube: part II – performance evaluation of draft tube model, *J. Glob. Optim.* 55 (4) (2013) 729–749. doi:10.1007/s10898-012-0011-4.
- [9] J. Bergström, Turbulence modeling and numerical accuracy for the simulation of the flow field in a curved channel, in: *Proceedings, 1997 ASME Fluid Engineering Division Summer Meeting : FEDSM97-3298, Symposium on Separated and Complex Flows*, 1997.
- [10] B. J., R. Gebart, Estimation of numerical accuracy for the flow field in a draft tube, *Int. J. Num. Meth. Heat & Fluid Flow* 9 (4) (1999) 472–487. doi:10.1108/09615539910266620.
- [11] I. Celik, W.-M. Zhang, Calculation of numerical uncertainty using richardson extrapolation: application to some simple turbulent flow calculations, *J. Fluids Eng.* 117 (3) (1995) 439–445.
- [12] I. Celik, U. Ghia, P. Roache, C. Freitas, H. Coleman, P. Raad, Procedure for estimation and reporting of uncertainty due to discretization in CFD

- applications, *J. Fluids Eng.* 130 (7) (2008) 078001–078001–4. doi:10.1115/1.2960953.
- [13] A. Abbas, A. Kumar, Development of draft tube in hydro-turbine: a review, *Int. J. Amb. Ener.* 38 (3) (2017) 323–330. doi:10.1080/01430750.2015.1111845.
- [14] T. Engström, L. Gustavsson, R. Karlsson (Eds.), *Proceedings of Turbine-99 – Workshop II*, Luleå University of Technology, Sweden, 2001.
- [15] M. Cervantes, M. Lövgren, Radial velocity at the inlet of the turbine-99 draft tube, in: *Proceedings of the 2nd IAHR International Meeting of the Workgroup on Cavitation and Dynamic Problems in Hydraulic Machinery and Systems*, Timisoara, Romania, October 24-26, 2007, no. 52(66) in *Transaction of Mechanics*, Scientific Bulletin of the Politehnica University of Timisoara, Romania, 2007, pp. 137–144.
- [16] D. Marjavaara, S. Lundström, Response surface-based shape optimization of a francis draft tube, *Int. J. Numer. Meth. Heat Fluid Flow* 17 (1) (2007) 34–45. doi:10.1108/09615530710716072.
- [17] B. R. Gebart, L. H. Gustavsson, R. I. Karlsson (Eds.), *Turbine-99: workshop on draft tube flow*, Luleå University of Technology, Sweden, 2000.
- [18] M. Cervantes, T. Engström, L. Gustavsson, *Proceedings of turbine-99 III: Workshop on draft tube flow*, Luleå University of Technology (2005).
- [19] N. Tanase, B. Florentina, G. Ciocan, Numerical simulation of the flow in the draft tube of the Kaplan turbine, *U.P.B. Sci. Bull., Series D* 74 (1) (2012) 83–90.
- [20] H. Nilsson, M. Cervantes, Effects of inlet boundary conditions, on the computed flow in the turbine-99 draft tube, using OpenFOAM and CFX, *IOP Conference Series: Earth and Environmental Science* 15 (3) (2012) 032002. doi:10.1088/1755-1315/15/3/032002.
- [21] Z. Čarija, Z. Mrša, L. Dragović, Turbulent flow simulation in kaplan draft tube, in: *5th International Congress of Croatian Society of Mechanics*, 2006.

- [22] S. Galván, M. Reggio, F. Guibault, Assessment study of k-e turbulence models and near-wall modeling for steady state swirling flow analysis in draft tube using fluent, *Eng. Appl. Comput. Fluid Mech.* 5 (4) (2011) 459–478. doi:10.1080/19942060.2011.11015386.
- [23] H. G. Weller, G. Tabor, H. Jasak, C. Fureby, A tensorial approach to computational continuum mechanics using object-oriented techniques, *J. Comput. Phys.* 12 (6) (1998) 620–631. doi:10.1063/1.168744.
- [24] R. Issa, Solution of the implicitly discretised fluid flow equations by operator-splitting, *J. Comput. Phys.* 62 (1) (1986) 40–65. doi:10.1016/0021-9991(86)90099-9.
- [25] S. Patankar, D. Spalding, A calculation procedure for heat, mass and momentum transfer in three-dimensional parabolic flows, *Int. J. Heat Mass Transf.* 15 (10) (1972) 1787–1806. doi:10.1016/B978-0-08-030937-8.50013-1.
- [26] U. Andersson, F. Engström, H. Gustavsson, R. Karlsson, The turbine-99 workshops - conclusions and recommendations, in: 22nd IAHR Symposium on Hydraulic Machinery and Systems, Stockholm, Sweden, June 29 - July 2, 2004, IAHR, 2004.
- [27] C. Michael, W. Torsten, Special interest group on quality and trust in industrial CFD. Best Practice Guidelines, European Research Community on Flow, Turbulence and Combustion (ERCOFTAC), 2000.
- [28] S. Galván, C. Rubio, J. Pacheco, C. Mendoza, M. Toledo, Optimization methodology assessment for the inlet velocity profile of a hydraulic turbine draft tube: part I – computer optimization techniques, *J. Glob. Optim.* 55 (1) (2013) 53–72. doi:10.1007/s10898-012-9946-8.
- [29] F. Juretić, cfmesh: Advanced meshing tool (2017).  
URL [cfMesh.com](http://cfMesh.com)
- [30] B. Marjavaara, T. Lundström, J. Wright, R. Kamakoti, S. Thakur, W. Shyy, Steady and unsteady CFD simulation of the turbine-99 draft tube using CFX and STREAM, in: Proceedings of the third IAHR/ERCOFTAC workshop on draft tube flow, no. 7, 2005, pp. 83–92.



- [31] U. Andersson, An experimental study of the flow in a sharp-heel draft tube, Ph.D. thesis, Luleå University of Technology, Sweden (2008).
- [32] T. Vekve, An experimental investigation of draft tube flow, Ph.D. thesis, Norwegian University of Science and Technology, Norway (2004).
- [33] M. Cervantes, T. Engström, Factorial design applied to CFD, *J. Fluids Eng.* 126 (5) (2004) 791–798. doi:10.1115/1.1792277.
- [34] T. Ran, Z. Xuezhi, X. Buchao, W. Zhengwei, Numerical investigation of the flow regime and cavitation in the vanes of reversible pump-turbine during pump mode’s starting up, *Renew. Energy* 141 (C) (2019) 9–19. doi:10.1016/j.renene.2019.03.
- [35] B. Mulu, P. Jonsson, M. Cervantes, Experimental investigation of a kaplan draft tube – part I: Best efficiency point, *Appl. Energy* 93 (2012) 695–706. doi:10.1016/j.apenergy.2012.01.004.
- [36] S. Daniels, A. Rahat, R. Everson, G. Tabor, J. Fieldsend, Shape optimisation of the sharp-keeled Kaplan draft tube: Part II - performance optimisation using a multi-objective Bayesian methodology, *Renew. Energy* (submitted).
- [37] E. Catmull, R. Rom, A class of local interpolating splines, in: R. Barnhill, R. Riesenfeld (Eds.), *Computer Aided Geometric Design*, Academic Press, 1974, pp. 317–326. doi:10.1016/B978-0-12-079050-0.50020-5.
- [38] P. Jonsson, B. Mulu, M. Cervantes, Experimental investigation of a kaplan draft tube – part II: Off-design conditions, *Appl. Energy* 94 (2012) 71–83. doi:10.1016/j.apenergy.2012.01.032.
- [39] N. Dahlbäck, Redesign of sharp heel draft tube – results from tests in model and prototype, in: E. Cabrera, V. Espert, F. Martínez (Eds.), *Hydraulic Machinery and Cavitation: Proceedings of the XVIII IAHR Symposium on Hydraulic Machinery and Cavitation*, Springer Netherlands, Dordrecht, 1996, pp. 985–993. doi:10.1007/978-94-010-9385-9\_100.

- [40] C. Duarte, F. de Souza, V. dos Santos, Mitigating elbow erosion with a vortex chamber, *Powder Technol.* 288 (2016) 6–25. doi:10.1016/j.powtec.2015.10.032.
- [41] Y. San, R. Thien, V. Chen, Numerical study on erosion of a pipe bend with a vortex chamber, *Particulate Science and Technology* 0 (0) (2018) 1–7. doi:10.1080/02726351.2017.1360973.
- [42] H. Ghafari, M. Sharifi, Numerical and experimental study of an innovative design of elbow in the pipe line of a pneumatic conveying system, *Powder Technol.* 331 (2018) 171–178. doi:10.1016/j.powtec.2018.03.022.